CHEMISTRY OF MATERIALS

pubs.acs.org/cm Article

Multivalent Ion Transport in Anti-Perovskite Solid Electrolytes

Kwangnam Kim and Donald J. Siegel*

Cite This: *Chem. Mater.* 2021, 33, 2187−2197 Read Online

ACCESS | Metrics & More | Article Recommendations | Supporting Information

ABSTRACT: Batteries based on the shuttling of multivalent (MV) ions are attractive energy storage systems due to their potential to transfer multiple electrons per working ion. Nevertheless, these batteries remain in an early stage of development, and performance improvements are desired for electrolytes that can transport MV ions efficiently and for cathode materials that can store MV ions at high capacity. The present study explores potential MV solid electrolytes (SEs) based on the anti-perovskite (AP) structure. Ten SE compositions are considered: Mg_3NX, Ca_3NX (where X = P, As, Sb, or Bi), Ca_3PSb, and Ca_3AsSb. First-principles calculations are used to predict several properties that are relevant for SE performance: stability, band gaps, elastic moduli, ion migration barriers, and defect formation energies. All compounds are predicted to be thermodynamically stable at 0 K. Similar to the monovalent AP SEs, lattice distortions in the MV systems decrease the energy barrier for percolating ion migration. Large energies associated with the formation of vacancies and interstitials imply that achieving high conductivities will require defect concentrations that are controlled via doping or composition variation. Of the compounds investigated, Mg_3NAs, Ca_3NAs, and Ca_3PSb are the most promising. These SEs are predicted to be stable against Mg or Ca anodes and have barriers for vacancy migration that are less than ∼500 meV (less than ∼200 meV for interstitial migration). Stability against oxidation is maintained up to 1.2−1.7 V, implying that interfacial coatings may be needed to achieve compatibility with high-voltage cathodes.

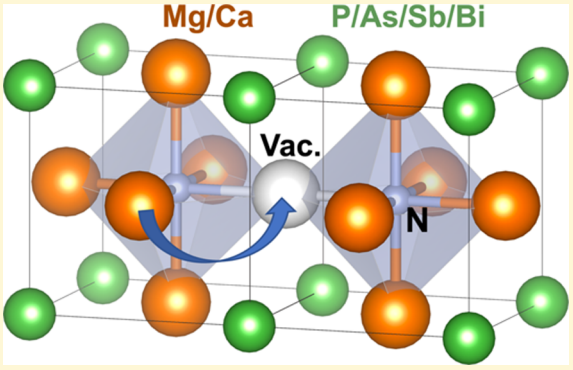

INTRODUCTION

Batteries based on multivalent (MV) working ions such as Mg, Ca, and Al have the potential to outperform today's Li-ion systems.[1] Nevertheless, MV batteries remain at an early stage of development. For example, in the case of Al-based systems, few suitable electrolyte and electrode materials exist.[1−3] In addition, the more positive standard potential of Al/Al^{3+}, which is 1.3 V more positive than Li/Li+, implies that high capacities must be achieved to compensate for potentially lower operating voltages. In contrast, the standard potentials of Ca/Ca^{2+} and Mg/Mg^{2+} are only 0.17 and 0.6 V more positive than Li/Li+, respectively.[1] Moreover, significant progress has been made in the development of electrolyte and cathode materials for rechargeable Mg-ion batteries.[4−8] Reversible electrodeposition of Ca has also been recently demonstrated.[2,9]

Improving the energy density and safety of batteries are widely acknowledged goals.[10] Safety hazards in Li-ion batteries can originate from the use of liquid electrolytes, which are volatile and flammable.[11] In principle, safety can be enhanced by substituting a solid electrolyte (SE) in place of the liquid.[12] Furthermore, SEs may enable the use of metallic anodes; metal anodes are projected to increase energy density significantly on both a mass and volume basis.[13,14]

An increasing number of inorganic SEs have been demonstrated to exhibit high conductivities for Li-ions at room temperature (R.T.). Examples include $Li_{2.9}PO_{3.3}N_{0.46}$,[15] $75Li_2S{\cdot}25P_2S_5$ (LPS glass),[16] $Li_7La_3Zr_2O_{12}$,[17] Li_6PS_5Br,[18] $Li_{10}GeP_2S_{12}$,[19] and $Li_{9.54}Si_{1.74}P_{1.44}S_{11.7}Cl_{0.3}$.[20] These materials open the door to realizing solid-state batteries (SSBs) that employ Li-metal as the anode (although several challenges associated with SE/electrode interfaces have yet to be resolved).[21] Several solid Na- and K-ion conductors are also known: Na_3PS_4 (glass−ceramic),[22] $Na_{10}SnP_2S_{12}$,[23] $Na_{11}Sn_2PS_{12}$,[24] $NaCB_{11}H_{12}$,[25] K-β''-Al_2O_3 (beta-alumina; also known to conduct Na, Ag, Li, and Rb ions),[26,27] and $K_2Fe_4O_7$.[28]

In contrast, few superionic MV SEs have been reported. In one instance, metal−organic frameworks (MOFs) were demonstrated as hosts for solid Mg conductors.[29] Using $Mg(OPhCF_3)_2$ and $Mg(TFSI)_2$ salts inserted into the MOFs Mg_2(dobdc) and Mg_2(dobpdc), Mg-ion conductivities up to 10^{-4} S/cm (activation energy E_a = 110−190 meV) were reported at R.T. Mg-polymer PEO−P[$(STFSI)_2Mg$] was also

Received: January 11, 2021
Revised: February 23, 2021
Published: March 8, 2021

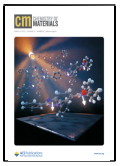

https://dx.doi.org/10.1021/acs.chemmater.1c00096
Chem. Mater. 2021, 33, 2187−2197

demonstrated with a conductivity of ~10^{-7} S/cm.[30] The first demonstration of fast Mg-ion conduction (~10^{-5} S/cm, E_a = 370 meV) at R.T. in a close-packed framework was reported in the mixed-conducting spinel, $MgSc_2Se_4$.[31] Zn-ion conductivities from 10^{-8} to 10^{-6} S/cm at 60 °C (E_a = 351 ± 99 meV) were reported in $ZnPS_3$.[32] In addition, Ca-ion conductivities up to 10^{-4} S/cm at R.T. (E_a = 310 meV; transference number = 0.359) have been reported in solid polymer electrolytes containing $Ca(NO_3)_2$ salt and generated by cross-linking PTHF and epoxy.[33,34]

Recently, anti-perovskites (APs) have been suggested as another promising class of SEs.[35,36] Monovalent APs adopt the formula X_3AB, where X is a monovalent cation and A and B are anions with respective charges of −2 and −1. The AP crystal structure consists of vertex-sharing X_6A octahedra with A situated at the octahedra centers. The octahedra are enclosed by a cubic framework with B anions at the vertices. Thus, the A and B anions together form a bcc lattice with the cations (X) at the center of the cube faces.

Several APs have been reported to exhibit both high conductivities for alkali-ions and large band gaps.[35−38] For example, the AP with composition Li_3OCl (later reported to be Li_2OHCl)[39] has demonstrated a conductivity for Li-ions of ~10^3 S/cm at R.T. and was predicted to have a large band gap of 8 eV.[35,37] Furthermore, a Li_3OCl-based cell based on a graphitic anode and $LiCoO_2$ cathode was shown to cycle at voltages up to 4.2 V.[40] Finally, measurements and calculations on Li/Li_3OCl interfaces concluded that Li_3OCl is compatible with a Li anode.[40−42]

Other AP compositions may be viable as solid electrolytes. For example, prior computational studies by the present authors explored 24 model alkali-metal-based APs, where X is Li or Na; A is O, S, or Se; and B is F, Cl, Br, or I. That work identified correlations between ion mobility, thermodynamic stability, and symmetry-lowering lattice distortions, of which the latter was quantified using the tolerance factor, *t*. Several unexplored AP compositions that strike a balance between ion mobility and stability were proposed.[37]

Beyond alkali metals, many alkaline earths, 3d transition metals, and lanthanides are known to occupy the cation sublattice in the AP structure.[43−57] These APs exhibit a wide range of electronic, magnetic, and thermal properties and have been examined for applications such as thermoelectrics, memory devices, sensors, and optical devices.[44,50] Nonalkali metal APs typically contain small, first-row anions (B, C, N, or O) positioned at the octahedron centers (A site), with a variety of other anions occupying the cubic framework (B) sites.

The present study predicts the performance of several Mg- and Ca-based APs as potential MV SEs. Ten compositions were examined, all of which are based on pnictogen anions (i.e., elements from group 15) with a formal charge of 3^- on the A and B sites: Ca_3PSb, Ca_3AsSb, $Mg_3N\Sigma$, and $Ca_3N\Sigma$,[46−49] where Σ is P, As, Sb, or Bi. Similar to the alkali metal APs, Mg^{2+} and Ca^{2+} cations in the MV AP occupy X sites at the vertices of the AX_6 octahedra. All 10 of the MV AP compositions examined here are nonmetallic and have been previously discussed in the literature, albeit not as SEs.[46−49] Six (i.e., Mg_3NAs, Mg_3NSb, Ca_3NP, Ca_3NAs, Ca_3NSb, and Ca_3NBi) have been successfully synthesized.[46,47,58]

Several properties of the MV APs that are relevant for SE performance were predicted using first-principles calculations: stability, band gaps, elastic moduli, ion migration barriers, and defect formation energies. All compounds are predicted to be thermodynamically stable at 0 K. Similar to the monovalent AP SE, lattice distortions in the MV systems decrease the energy barrier for percolating ion migration. Large energies associated with the formation of vacancies and interstitials imply that achieving high conductivities will require that defect concentrations are controlled via doping or composition variation.

Of the compounds investigated, Mg_3NAs, Ca_3NAs, and Ca_3PSb are the most promising. These SEs are predicted to be stable against their respective metal anodes and have percolating barriers for vacancy migration of less than ~500 meV (~200 meV for interstitial migration). Stability against oxidation is maintained up to 1.2−1.7 V, implying that interfacial coatings may be needed to achieve compatibility with high-voltage cathodes.

METHODS

DFT calculations were performed using the Vienna *ab initio* Simulation Package (VASP).[59] The Perdew−Burke−Ernzerhof (PBE)[60] exchange-correlation functional was used in combination with the projector augmented wave (PAW) method.[61,62] The valence electron configurations were $2s^22p^63s^2$ for Mg, $3s^23p^64s^2$ for Ca, $2s^22p^3$ for N, $3s^23p^3$ for P, $4s^24p^3$ for As, $4d^{10}5s^25p^3$ for Sb, and $5d^{10}6s^26p^3$ for Bi. The plane-wave basis included functions with kinetic energies of at least 550 eV for Mg-containing compounds and at least 450 eV for Ca-based compounds. (To ensure consistency with calculated data in the Materials Project, a cutoff energy of 520 eV was used for all compounds for phase diagram and chemical stability assessments.)

The Brillouin zone was sampled using an 8 × 8 × 8 grid for cubic Mg APs (5 atoms per primitive cell), a 6 × 6 × 6 grid for cubic Ca APs (5 atoms per primitive cell), and a 3 × 3 × 3 grid for all orthorhombic APs (20 atoms per cell). In all cases, a Γ-centered *k*-point mesh was used. These cutoff energies and *k*-point sampling densities yielded energy convergence to within 2 meV/atom. The energy criterion for convergence of the self-consistency loop was set to 10^{-5} eV, and the force criterion for the relaxation of geometric degrees of freedom (ion positions and cell geometry) was 0.01 eV/Å. Additional details regarding convergence criteria used for other materials can be found in the Supporting Information. The equilibrium volumes of all systems were determined by fitting energy data as a function of volume to the Murnaghan equation of state.[63] Band gaps were calculated using the non-self-consistent GW (G_0W_0) method; wave functions used as inputs to G_0W_0 calculations were determined from self-consistent HSE06[64,65] hybrid functional calculations.[66−68]

Energy barriers for ion migration were evaluated with the nudged elastic band (NEB) method.[69,70] NEB calculations were performed on enlarged supercells based on a 3 × 3 × 3 replication (135 atoms) of the unit cell for cubic (space group *Pm*-3*m*) compounds and a 2 × 2 × 2 replication (160 atoms) for orthorhombic systems (space group *Pnma*). The Brillouin zone was sampled using a 2 × 2 × 2 (2 × 2 × 1) grid for cubic (orthorhombic) supercells. These sampling densities yielded energy barriers that are converged to within 1 meV/atom. The force convergence criterion for NEB calculations was set to 0.04 eV/Å, and three intermediate images were used.

Bulk and shear moduli were determined from the Voigt equations using calculated stiffness tensors, C_{ij}, as[71]

$$B = [(C_{11} + C_{22} + C_{33}) + 2(C_{12} + C_{13} + C_{23})]/9$$

$$S = [(C_{11} + C_{22} + C_{33}) - (C_{12} + C_{13} + C_{23}) + 3(C_{44} + C_{55} + C_{66})]/15$$

Bulk moduli determined from the Voigt equation are similar to those obtained from the Murnaghan equation (see Table 2). Finite differences were used to evaluate the stiffness tensor from the strain−stress relationship, as implemented in the VASP. Larger cutoff

https://dx.doi.org/10.1021/acs.chemmater.1c00096
Chem. Mater. 2021, 33, 2187−2197

energies and denser k-point sampling densities were used to evaluate the stiffness tensors. Additional details are provided in the Supporting Information.

The present study examines the mobility of MV ions assuming that their migration is mediated by vacancies and interstitials. The formation energy of a defect X with charge state q (i.e., X^q) is given by[72]

$$E_f(X^q) = E_0(X^q) - E_0(\text{bulk}) - \sum_i n_i\mu_i + q\varepsilon_F + E_{MP1}$$

where $E_0(X^q)$ and $E_0(\text{bulk})$ are the total energies of the defective and pristine bulk supercells, respectively, n_i and μ_i denote the number and chemical potential of a species i that has been added to or removed from the cell in the course of creating the defect, respectively, ε_F is the Fermi level referenced to the valence band maximum, and E_{MP1} is the Makov−Payne (MP) finite-size correction for charged systems.[73,74] The MP correction term was evaluated using the respective macroscopic dielectric constants, calculated here to be 28.4, 35.8, 29.6, and 33.2 for $Mg_3N\Sigma$, where Σ is P, As, Sb, and Bi, respectively; 23.8, 28.5, 26.7, and 29.2 for $Ca_3N\Sigma$, where Σ is P, As, Sb, and Bi, respectively; and 19.6 and 35.2 for Ca_3ASb, where A is P and As, respectively. (More stringent DFT settings equivalent to those used for elastic modulus calculations were adopted for the dielectric constant calculations.) ε_F was determined by the charge neutrality condition, $\sum_{X^q} qC(X^q) = 0$, where $C(X^q) = D_{X^q}e^{-E_f(X^q)/k_BT}$ is the equilibrium concentration of defect X^q [D_{X^q} is the number of (symmetry-equivalent) available defect sites per unit volume, k_B is the Boltzmann constant, and T is the absolute temperature].[72] The chemical potential of Ca or Mg metal at the metal anode is given by $\mu_{i=\text{Ca or Mg}} = E(\text{Ca or Mg metal})$ equivalent to the energy per atom of FCC Ca or HCP Mg.

The phase diagram for the MV APs at 0 K was predicted using the Materials Project database, the *pymatgen* code, and the energies of phases determined using the present DFT calculations (which are not present in the Materials Project database).[75−78] The stability against oxidation/reduction of APs in contact with an electrode (i.e., its chemical stability window) was investigated as a function of potential (at 0 K, neglecting vibrational and pV contributions) using the grand potential phase diagram as[75,76]

$$E_{d,\text{open}}(\phi) = E_{\text{Phase equilibrium}}(\phi) - [E_{AP} + \Delta n_M\mu_M(\phi)]$$

where $E_{\text{Phase equilibrium}}(\phi)$ is the total energy of possible competing phases (formed from reaction of an AP with the electrode), E_{AP} is the energy of AP, Δn_M is the change in the number of metal atoms associated with the reaction (M = Mg or Ca metal), and μ_M is the chemical potential of M, defined as[79]

$$\mu_M(\phi) = \mu_M^0 - ze\phi$$

Here, μ_M^0 is the chemical potential of M in the absence of an applied potential (i.e., the bulk energy per atom of M), z is the charge on M ($z = +2$), and e is the electron charge. This analysis can identify the voltage range(s) associated with potential reduction ($\Delta n_M > 0$) and oxidation ($\Delta n_M < 0$) reactions involving an AP and resulting in the formation of new phases/compounds.

RESULTS AND DISCUSSION

Structure. The ground-state crystal structures were predicted for the six compounds that have been previously synthesized, i.e., Mg_3NAs, Mg_3NSb, Ca_3NP, Ca_3NAs, Ca_3NSb, and Ca_3NBi.[46,47,58] The atomic configuration of orthorhombic Ca_3NAs was used as an initial guess to the orthorhombic structure of Ca_3NP since for the latter compound, only the lattice parameter is experimentally known. The remaining four compounds exhibit cubic crystal structures.

Table 1 summarizes the predicted tolerance factors and lattice parameters. (The ionic radii used in the calculation of the tolerance factor are from Emsley;[80] see the Supporting Information for details regarding the ionic radius of Bi^{3-}.) The predicted structures are in good agreement with the experimental data. For example, the predicted tilt angle of the Ca−N octahedron (8.7°) in Ca_3NAs is nearly the same as that measured by experiments (8.8°).[58]

Table 1. Tolerance Factors (t), Crystal Structure Symmetries, and Lattice Parameters of Mg and Ca Anti-Perovskites[a]

compound	t	symmetry	a (Å)	b (Å)	c (Å)
Mg_3NP	0.823	orthorhombic	5.936	5.929	8.382
Mg_3NAs	0.851	cubic	4.242 (4.217)		
Mg_3NSb	0.916	cubic	4.378 (4.352)		
Mg_3NBi	0.925	cubic	4.437		
Ca_3NP	0.812	orthorhombic	6.742 (6.709)	6.627 (6.658)	9.433 (9.452)
Ca_3NAs	0.837	orthorhombic	6.733 (6.725)	6.728 (6.720)	9.550 (9.534)
Ca_3NSb	0.896	cubic	4.863 (4.854)		
Ca_3NBi	0.904	cubic	4.908 (4.888)		
Ca_3PSb	0.780	orthorhombic	7.434	7.813	10.599
Ca_3AsSb	0.757	orthorhombic	7.526	7.983	10.711

[a]Values in parentheses are experimental data.[46,47]

Regarding the remaining four (hypothetical) compounds (Mg_3NP, Mg_3NBi, Ca_3PSb, and Ca_3AsSb),[48,49] prior DFT studies modeled these systems assuming cubic symmetry. A subsequent DFT study showed that Mg_3NP may instead adopt an orthorhombic unit cell.[81] Here, both cubic and orthorhombic symmetries were examined. As previously described, the Ca_3NAs structure was used as a template for the orthorhombic systems.

The calculated structural data for the hypothetical APs in Table 1 indicates that only Mg_3NBi prefers the cubic structure. This agrees with its high tolerance factor of 0.925, which is the largest among the APs examined here. Consistent with their lower tolerance, the remaining hypothetical APs, Mg_3NP, Ca_3AsSb, and Ca_3PSb, all adopt the orthorhombic structure. Orthorhombic Mg_3NP is 15 meV/atom more stable than the cubic phase; its Mg−N octahedra exhibit a small tilting angle of 10°. Larger tilt angles of 18 and 21° are observed for Ca_3PSb and Ca_3AsSb, respectively. The orthorhombic structures of these compounds are more stable than the cubic variants by 106 and 162 meV/atom, respectively.

Similar to the monovalent APs,[37] where compounds with $t >$ 0.83 adopted cubic crystal structures, in the MV Mg- and Ca-based AP compounds, a preference for cubic symmetry is observed for $t > 0.84$. The similarities with the monovalent APs also extend to the MV APs with lower tolerance. In a prior study,[37] we reported that APs with tolerance values between 0.72 and 0.83 exhibit moderate tilting of the cation octahedra. This same behavior appears in the MV APs that have lower t.

Thermodynamic Stability. Figure 1 shows the calculated ternary phase diagrams for the 10 MV APs considered here. All are predicted to be stable at 0 K. These predictions are in agreement with the fact that six of the 10 compounds have been synthesized previously (Table 2).[46,47] This data also suggests that the remaining four compounds may also be synthesizable.

Percolating Barrier for Ion Migration. Cation vacancies and interstitial dumbbells have been suggested as the defects

https://dx.doi.org/10.1021/acs.chemmater.1c00096
Chem. Mater. 2021, 33, 2187−2197

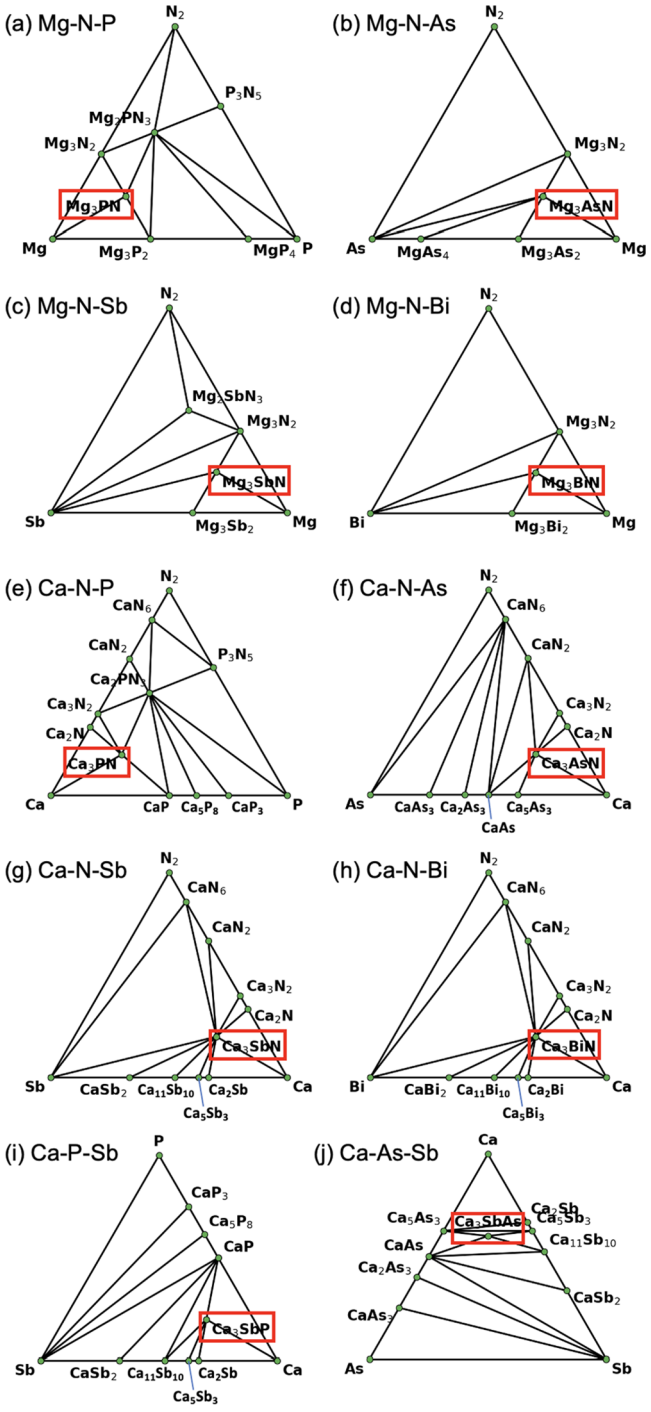

Figure 1. Calculated ternary phase diagrams for (a−d) Mg- and (e−j) Ca-based APs.

that mediate cation mobility in the AP lattice.[82−87] These defects reside on/near the vertices of the cation octahedra and migrate along the octahedron edges, resulting in a total of 12 possible elementary pathways for ion migration (corresponding to the 12 edges of an octahedron). Due to the high symmetry of the cubic APs, all 12 paths are equivalent in systems with cubic symmetry. In the lower-symmetry orthorhombic systems, tilting of the octahedra breaks this degeneracy; hence, in these systems, the elementary migration pathways can exhibit distinct barriers.[37] Based on an evaluation of all elementary migration barriers along the octahedral edges, the minimum energy barrier for long-range migration, referred to as the *limiting barrier*, was calculated using percolation theory as informed by the connectivity between octahedra and the spectrum of elementary barriers (see elsewhere[37] for additional details). In cubic APs, the elementary and limiting barriers are the same.

Figure 2a,b presents the distribution of elementary energy barriers across the examined APs as a function of their tolerance. As previously described, lattice distortions present in the noncubic APs result in a spectrum of elementary barriers for these compounds; the lower limit of the barrier spectrum decreases in a roughly linear fashion with decreasing tolerance, while the upper limit increases more rapidly, similar to what was reported for monovalent APs.[37] (One exception is the lower-energy barriers for the dumbbell mechanism in Ca_3AsSb. Here, some defect sites were found to be unfavorable in that interstitials created at these sites relaxed to other sites.)

One important difference between the MV and monovalent APs relates to the lower limit of the spectrum of elementary barriers: in the MV APs, these barriers are larger than those of the monovalent APs. For example, the lower limits for the barriers in the MV AP at t ∼0.75 are 300 and 100 meV for vacancy and dumbbell migration, respectively. In contrast, in the monovalent AP, these barriers (at t ∼0.75) are approximately 200 and 50 meV.[37] The observation of larger barriers associated with the migration of MV ions is consistent with a prior report.[88] In addition, the width of the spectrum of elementary barriers (defined as the difference between the largest and smallest energy barriers for a given compound) is larger in the MV APs than for the monovalent APs reported elsewhere.[37] For example, for APs having t ∼0.75, the spectrum of vacancy barriers for the MV systems ranges from 300 to 1000 meV. For the monovalent APs, a much narrower range of 150 to 400 meV was reported.[37] A similar trend is observed for the elementary barriers associated with interstitial migration.

Based on the calculated elementary barriers, Figure 2c,d illustrates the minimum energy pathways for percolating MV ion migration for vacancy and interstitial dumbbell mechanisms, respectively. An example of a long-range migration pathway is shown in Figure S2. The limiting barrier corresponds to the largest energy along a given pathway. Assuming a vacancy mechanism, the limiting barriers range from 373 meV in Ca_3AsSb to 900 meV in Ca_3NBi. The limiting barriers are smaller for the interstitial mechanism, ranging from 132 meV in Ca_3NP to 706 meV in Mg_3NBi (Table 2). Furthermore, the limiting barriers decrease with decreasing tolerance; this behavior is expected from the decrease in the lower limit of the spectrum of elementary barriers (Figure 2a,b) and is similar to what was observed in monovalent APs.[37]

Overall, the limiting barriers predicted here for the MV APs are larger than those reported for the monovalent APs: MV barriers range from 373 to 900 meV for vacancy migration and 132 to 706 meV for the dumbbell mechanism, while in the monovalent APs, these values are 200−400 (vacancy) and 50−200 meV (dumbbell) for APs having the same range of tolerance factors (i.e., t > 0.75).[37] Nevertheless, several of the MV APs exhibit limiting barriers for vacancy migration that are less than the 525 meV threshold, which has been proposed to allow for C/2 charging/discharging.[88] These include Mg_3NP, Mg_3NAs, Ca_3NP, Ca_3NAs, Ca_3PSb, and Ca_3AsSb. In addition, limiting barriers below 200 meV are predicted for the

https://dx.doi.org/10.1021/acs.chemmater.1c00096
Chem. Mater. 2021, 33, 2187−2197

Table 2. Summary of Predicted Properties of Mg and Ca AP Compounds[a]

			limiting barrier (meV)				modulus (GPa)	
compound	t	thermodynamic stability	vacancy	dumbbell	chemical stability window (V)	band gap (eV)	bulk	shear
Mg_3NP	0.823	stable	517	162	0.01 to 0.52	2.79	90.5 (89.1)	69.6
Mg_3NAs	0.851	stable (synthesized)[47]	519	195	−0.41 to 1.18	2.68	87.9 (84.9)	71.7
Mg_3NSb	0.916	stable (synthesized)[47]	759	246	0.02 to 0.78	1.78	80.3 (78.2)	62.1
Mg_3NBi	0.925	stable	723	706	0.02 to 0.39	1.59	74.3 (72.1)	55.5
Ca_3NP	0.812	stable (synthesized)[46]	446	132	−2.22 to 0.92	2.68	62.0 (62.5)	42.6
Ca_3NAs	0.837	stable (synthesized)[46]	508	171	−0.38 to 1.68	2.14	60.0 (60.9)	45.7
Ca_3NSb	0.896	stable (synthesized)[46]	865	233	−0.57 to 1.85	1.70	57.8 (57.9)	49.5
Ca_3NBi	0.904	stable (synthesized)[46]	900	247	−0.56 to 1.71	1.65	54.1 (54.1)	47.0
Ca_3PSb	0.780	stable	433	206	−1.99 to 1.41	2.14	39.8 (40.1)	21.1
Ca_3AsSb	0.757	stable	373	321	0.64 to 1.33	2.00	36.9 (36.8)	18.0

[a]The bulk modulus in parentheses is a value predicted by the Murnaghan EOS fitting. The chemical stability window is reported with respect to the potential for Mg/Mg^{2+} or Ca/Ca^{2+}.

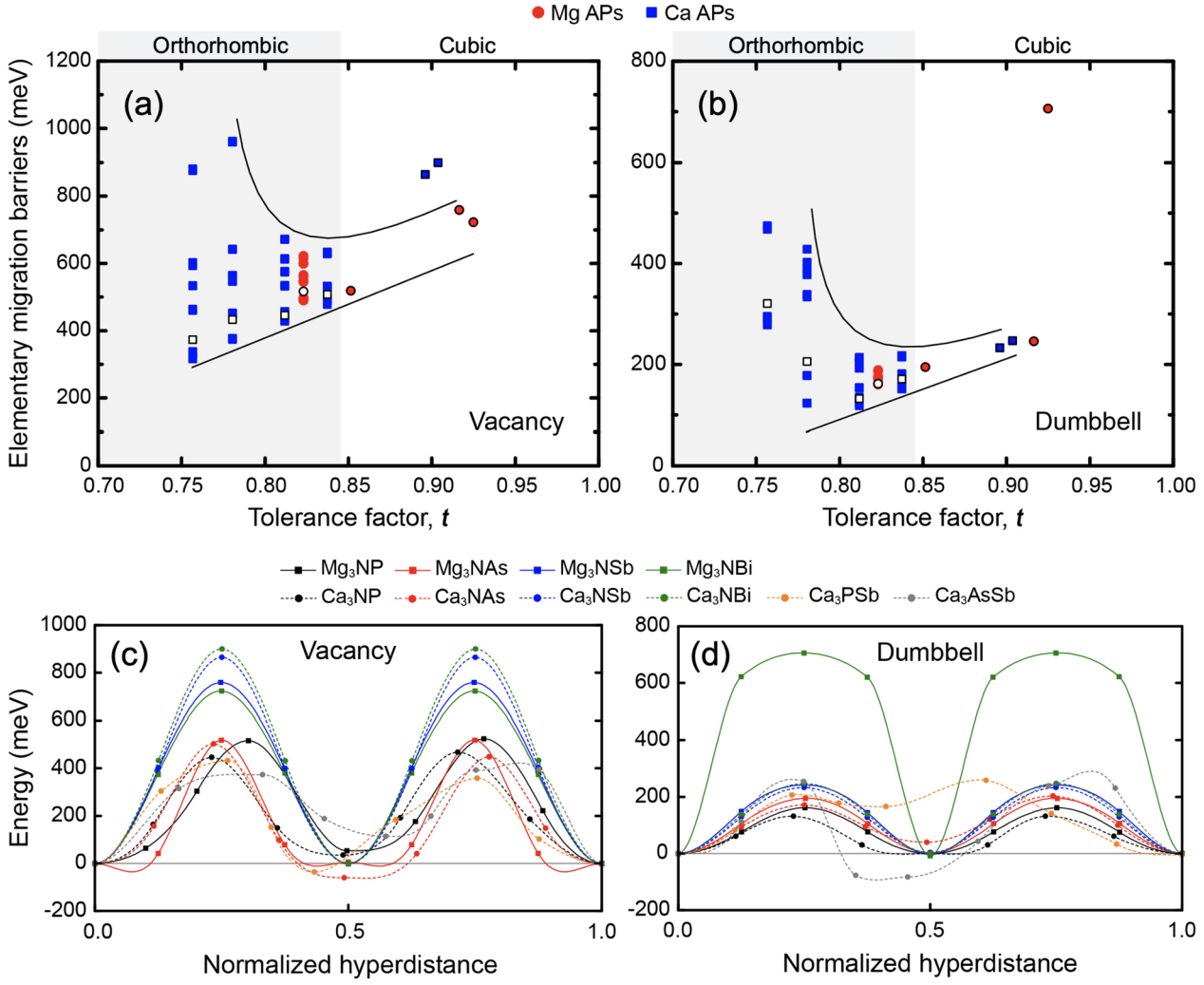

Figure 2. Calculated energy barriers for ion migration in MV APs. (a,b) Distribution of elementary barriers as a function of the tolerance t for (a) vacancy and (b) interstitial dumbbell migration mechanisms. Black lines highlight the increasing range of the barriers with decreasing tolerance. Open data points denote the respective limiting barriers. (c,d) Minimum energy pathways for percolating ion migration for vacancy (c) and interstitial dumbbell mechanisms. The limiting barrier corresponds to the difference between the maximum and minimum energies along a given pathway. Note that the energy along the path is plotted relative to the initial energy; thus, in some cases, the energy can be negative [e.g., gray dotted line in panel (d) for Ca_3AsSb].

dumbbell mechanism in several MV APs, including Mg_3NP, Mg_3NAs, Ca_3NP, and Ca_3NAs. These values are comparable to state-of-the-art MV SEs such as $MgSc_2Se_4$ (calculated barrier of 375 meV; experimental activation energy of 370 ± 90 meV), PEGDA-Ca (experimental activation energy = 221−282 meV depending on the Ca-salt loading level), and $ZnPS_3$

https://dx.doi.org/10.1021/acs.chemmater.1c00096
Chem. Mater. 2021, 33, 2187−2197

Table 3. Formation Energies of Six Categories of Defects in Mg and Ca APs (for Comparison, Literature Values for Li_3OCl Are Also Reported)[a]

		defect formation energy (eV per defect)						
compounds	t	neutral vacancy	neutral interstitial	charged vacancy/interstitial	Frenkel	X_3AB Schottky	X_xA_y Schottky	X_xB_y Schottky
Li_3OCl	0.823			1.3[87]	1.59[84]	1.44[84]	1.56[84]	0.93*[84]
Mg_3NP	0.823	3.46*	4.53	3.76	4.33	8.53	9.09	8.26
Mg_3NAs	0.851	2.84*	4.57	4.66	4.22	7.34	7.91	7.04
Mg_3NSb	0.916	2.57*	4.45	6.82	5.05	7.08	6.63	7.77
Mg_3NBi	0.925	2.14*	4.44	5.24	4.87	6.17	5.16	7.07
Ca_3NP	0.812	3.89	3.36*	4.18	4.35	8.97	6.61	3.93
Ca_3NAs	0.837	3.30	3.20*	4.09	4.14	8.46	6.02	3.93
Ca_3NSb	0.896	3.31*	3.65	4.46	5.44	8.70	5.88	9.70
Ca_3NBi	0.904	5.53	8.45	11.05	5.54	6.70	3.13*	3.87
Ca_3PSb	0.780	4.20	1.53*	5.62	3.23	8.98	7.73	6.57
Ca_3AsSb	0.757	3.91	1.20*	3.23	2.73	8.28	3.56	6.09

[a]Asterisks indicate defects having the smallest formation energies for a given AP composition. See Figure S1 for plots of the formation energy vs Fermi level.

(experimental activation energy of 351 ± 99 meV).[31−33] It is possible that the limiting barrier can be further reduced in other MV compositions that exhibit larger lattice distortions (i.e., lower tolerance) or that have rotationally active complex anions (i.e., the paddle-wheel effect).[89]

Defect Formation Energies. Ultimately, it is the *conductivity* of the cations that is of the most importance in the design of solid electrolytes. The conductivity, σ, can be expressed as the product

$$\sigma = cZe\mu \quad (1)$$

where c is the concentration of carriers, Z is the valence of the migrating ion (2+ in the present case), e is the electron charge, and μ is the mobility.

The present discussion has thus far focused on predicting the energy barriers associated with ion migration. These barriers impact the mobility, μ. Nevertheless, as shown in eq 1, a full description of the conductivity requires knowledge of the carrier concentration (or, in the case of defect-mediated transport, the concentration of defects such as vacancies or interstitials) c.

In equilibrium, the concentration of defects can be expressed as $c \propto e^{-E_f/k_BT}$, where E_f is the formation energy associated with a given defect type. More explicitly, eq 1 can be expressed in terms of the diffusion coefficient, D, as $\sigma = \frac{cZ^2e^2D}{kT}$, where D in turn depends on the sum of the formation and migration energies:[90] $D = D_0\exp\left(\frac{-(E_m + E_f)}{kT}\right)$.

Previous studies have suggested that the formation energies for defects in the Li-based AP Li_3OCl are large (0.93 eV or larger, Table 3). Consequently, the concentration of thermally generated defects will be low, as will be the conductivity.[83,84,86,87] Therefore, alternative strategies for increasing the carrier concentration have been employed. These include the use of nonstoichiometric synthesis reactions (e.g., $Li_2O + (1 - x)LiCl \rightarrow Li_{3-x}OCl_{1-x}$) and by Sr^{2+} doping, as demonstrated, for example, in Na-based APs.[35,36]

Here, the formation energies of various defects in the MV APs have been calculated. These data reveal whether the equilibrium concentrations of thermally generated defects are sufficient to achieve high ionic conductivities or, alternatively, point to the need for defect incorporation during synthesis and/or via doping.

The energetics of neutral cation vacancies and interstitial dumbbells were characterized by removing or adding a Mg/Ca atom to/from the supercell. Charged versions of these defects were also considered, as were Frenkel and Schottky defects. A Frenkel defect comprises a vacancy-interstitial pair,[91] while Schottky defects comprise a set of vacancies formed by removing cations and anions in a neutral unit of $X_3A\Sigma$, X_xA_y, or $X_x\Sigma_y$ (see the Supporting Information for more details regarding the composition of Schottky defects).[91]

For simplicity, it is assumed that the formation energies for polarons are high and therefore do not impact the concentrations of ionic defects.[92]

Table 3 summarizes the calculated defect formation energies for the MV APs. In all cases, the formation energies are large, with the smallest energies falling within a range of 1.2−3.5 eV. With one exception, the smallest formation energies are generally associated with neutral vacancies or interstitials. The calculated values for the MV APs are larger than those reported for the LiCl Schottky defect in Li_3OCl (0.93 eV) and suggest that the equilibrium concentration of defects in the MV APs will be negligible at room temperature. Consequently, to achieve a high ionic conductivity, it is suggested that the carrier concentration in the MV AP be controlled via doping or through nonstoichiometric synthesis reactions. These strategies could mimic those used to generate vacancies on the Li-sublattice in $Li_{3-x}OCl_{1-x}$[34] or involve aliovalent substitution[35] of (e.g.) monovalent halogens for pnictogen anions.

Chemical Stability Window. An ideal SE will not react with the electrodes. To assess the likelihood for reaction with the electrodes, Figure 3 plots the calculated range of stabilities of the MV APs examined here as a function of potential (also see Table 2). Regarding reductive stability at low potentials, Figure 3 shows that all of the Mg APs are either absolutely stable against a Mg anode (i.e., in Mg_3NAs, the limit extends to 0 V with respect to Mg/Mg^{2+}) or are very weakly unstable (Mg_3NP, Mg_3NSb, and Mg_3NBi). In the latter case, the APs become unstable only at voltages below ∼0.02 V vs Mg/Mg^{2+}. Similarly, all of the Ca-based APs except Ca_3AsSb are predicted to be stable in contact with Ca metal anodes. Overall, the Mg and Ca APs exhibit good stability with their respective metal anodes.

The predicted limit for oxidative stability of the MV APs corresponds to the right edge of the horizontal bars in Figure 3. For the Mg APs, these limits range from 0.39 V at worst to

https://dx.doi.org/10.1021/acs.chemmater.1c00096
Chem. Mater. 2021, 33, 2187−2197

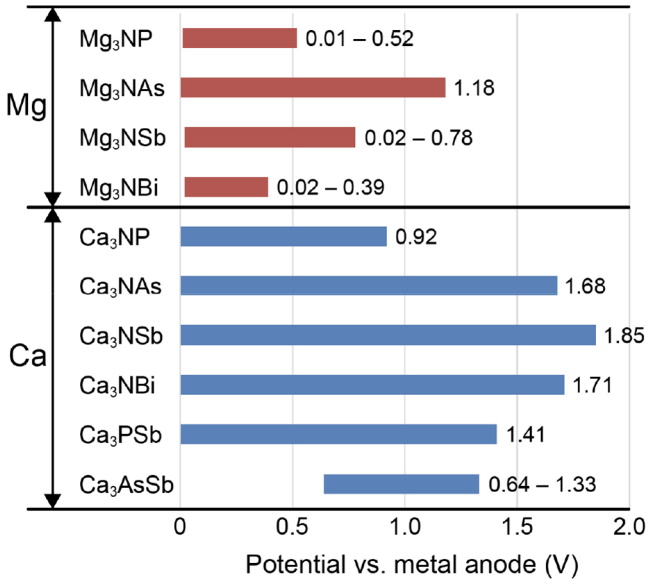

Figure 3. Chemical stability window of Mg- and Ca-based APs as a function of potential (with respect to Mg/Mg^{2+} or Ca/Ca^{2+}). The left edge of each horizontal bar represents the limit of stability with respect to reduction; the right edge represents the oxidative limit.

1.18 V at best (larger values are better). The Ca APs exhibit somewhat better resistance to oxidation; their stability windows extend from 0.92 V in the worst case (Ca_3NP) to, at best, 1.85 V for Ca_3NSb. To place these values in context, we note that the potentials of Mg cathodes such as Ti_2S_4, V_2O_5, and Mn_2O_4[7,93,94] range from 1.5 to 3 V. These values are all more positive than the most stable Mg AP, Mg_3NAs, whose oxidative stability limit was predicted to be 1.18 V. Similarly, Ca-based cathodes such as V_2O_5, Co oxides, and $MnFe(CN)_6$ operate at voltages of ~3 V vs Ca/Ca^{2+},[95−97] which is well above the limit exhibited by even the most stable Ca AP (1.85 V for Ca_3NSb). Therefore, even though the present APs exhibit good stability against their respective anodes, their stability at oxidizing potentials can be a limitation. Use of a coating between the SE and cathode could address this shortcoming.[98,99]

The standard potential for Ca/Ca^{2+} is more negative than that of Mg/Mg^{2+} by ~0.5 V. This implies that the driving force for reduction of an SE in contact with a Ca anode will be greater than for an SE in contact with a Mg anode and, by extension, that SEs in contact with Ca anodes will be less stable. Our calculations suggest that this is generally not the case for the APs considered here. Specifically, Table 2 shows that nearly all of the Ca-based APs have stability windows that extend to potentials that are more negative than those for their Mg-based counterparts. This apparent discrepancy can be understood by recognizing that stability is determined by the relative energetics of the electrode, the SE, and those of any new phases that form from the reduction reaction.[79] Thus, knowledge of the standard potential of the electrode is in itself insufficient for understanding stability.

Band Gap. A large band gap is a desirable feature for an SE because it can minimize harmful electronic charge transfer (electrons or holes) to/from the electrodes.[10,42,100,101] Here, quasi-particle (GW) calculations were used to predict the band gaps of the Mg and Ca APs examined in the present study. The band gap data are summarized in Table 2 and fall within a range of 1.65 to 2.79 eV. Although these values are smaller than those of other SEs, for example, LLZO has a bandgap of approximately 6 eV,[37,42,102] they still fall safely within the range of semiconducting behavior. (Ultimately, it is the positions of the band edges that more accurately determine if stability with respect to charge injection is a concern.)[101] The band gaps for the MV APs are observed to increase with decreasing anion size: for example, the band gaps of the Ca AP $Ca_3N\Sigma$ increase as Σ is varied according to Bi → Sb → As → P. This trend is in good agreement with a previous study.[46]

Elastic Properties. Monroe and Newman have proposed that the mechanical properties of an SE can influence the tendency for dendrites to form at the anode/SE interface.[13] More specifically, it was proposed that dendrite initiation may be suppressed if the SE has a shear modulus that is approximately twice larger than that of the anode.[13] In the spirit of applying the Monroe and Newman model, the bulk and shear moduli of the Mg and Ca APs have been calculated (Table 2) to estimate their ability to suppress dendrites. Overall, the Mg APs are predicted to be stiffer than the Ca-based systems: the bulk moduli in the Mg APs range from 74 to 90 GPa, while the shear modulus spans 55−69 GPa. These values are larger than the respective moduli in the Ca APs: 37−62 (bulk) and 18−43 GPa (shear). Compared to other noteworthy SEs, the moduli of the APs examined here exhibit intermediate values. For example, the MV APs are softer than $Li_7La_3Zr_2O_{12}$ (LLZO), which has bulk and shear moduli of ~100 and 60 GPa, respectively,[103,104] yet are stiffer than $Li_2S-P_2S_5$ (LPS) glass (20 GPa bulk, 8 GPa shear).[105,106]

To estimate the ability of the MV AP SE to suppress dendrite formation, knowledge of the shear modulus of the metal anode is also needed. The shear moduli of Mg and Ca metals have been previously measured and calculated.[107−109] The reported values for Ca are approximately 9 GPa, while ~17 GPa has been reported for Mg. Both of these values are at least twice smaller than the corresponding shear moduli for the APs, suggesting that (in the context of the Monroe and Newman model) the MV APs should be able to suppress dendrite initiation during plating. Nevertheless, factors beyond elastic properties alone can also strongly impact the ability of a given SE to suppress dendrites.[110]

Discussion. Which of the MV APs are the most promising? Taking into account all of the properties that have been examined here − ion mobility, formation energies, stability, band gaps, and elastic moduli − Mg_3NAs, Ca_3NAs, and Ca_3PSb are suggested as the compositions most worthy of experimental scrutiny. The properties of these compounds are summarized in a radar chart (Figure 4). These SEs possess a good combination of low migration barriers and stability against their respective metal anodes. Both Mg_3NAs and Ca_3NAs have been experimentally synthesized. Ca_3PSb is a hypothetical compound; nevertheless, it is predicted to be thermodynamically stable. Although the stability of these APs at high potentials is insufficient for use with high-voltage cathodes, their oxidative stabilities are among the best of the compositions examined and can potentially be improved with the use of a coating between the SE and cathode. Given that all of the MV APs exhibit high defect formation energies, achieving high conductivities will likely require that the defect concentration be controlled via doping or by the use of nonstoichiometric reactant mixtures.

Inspired by the promising properties of Ca_3PSb, we also briefly explored the hypothetical APs Mg_3PSb and Mg_3AsSb. Similar to their Ca analogues, these compounds are predicted

https://dx.doi.org/10.1021/acs.chemmater.1c00096
Chem. Mater. 2021, 33, 2187−2197

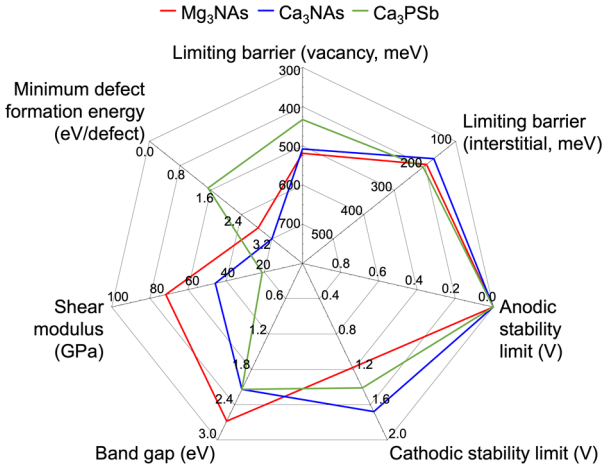

Figure 4. Radar chart summarizing the properties of Mg_3NAs (red), Ca_3NAs (blue), and Ca_3PSb (green) that are suggested as potential Mg and Ca SEs.

to exhibit orthorhombic symmetry (lattice parameters *a*, *b*, and *c* of 6.95, 6.86, and 9.91 Å for Mg_3PSb and 7.06, 6.97, and 10.24 Å for Mg_3AsSb, respectively). Unfortunately, neither compound is predicted to be stable at 0 K with respect to the Mg pnictogenides: Mg_3PSb should decompose into a mixture of Mg_3P_2 and Mg_3Sb_2 with an exothermic reaction energy of −35 meV/atom, while Mg_3AsSb is unstable with respect to Mg_3As_2 + Mg_3Sb_2 by −50 meV/atom. Furthermore, both compounds have a narrow window of chemical stability: a reduction potential limit of 0.02 V and an oxidation potential limit of 0.61 V. Hence, even if these materials could be synthesized, their poor oxidative stabilities would likely limit their utility as solid electrolytes.

CONCLUSIONS

The present study has predicted the performance of several Mg- and Ca-based anti-perovskites as potential multivalent solid electrolytes. Ten compositions were examined in detail: Mg_3NP, Mg_3NAs, Mg_3NSb, Mg_3NBi, Ca_3NP, Ca_3NAs, Ca_3NSb, Ca_3NBi, Ca_3PSb, and Ca_3AsSb (with two additional unstable compositions, Mg_3PSb and Mg_3AsSb, explored more briefly).[46−49] All 10 have been previously discussed in the literature, albeit not as SEs.[46−49] According to prior reports, six (i.e., Mg_3NAs, Mg_3NSb, Ca_3NP, Ca_3NAs, Ca_3NSb, and Ca_3NBi) have been successfully synthesized.[46,47,58]

Several properties of these materials were predicted using first-principles calculations: stability, band gaps, elastic moduli, ion migration barriers, and defect formation energies. All compounds are predicted to be thermodynamically stable at 0 K. Similar to the monovalent AP SEs, lattice distortions in the MV systems decrease the energy barrier for percolating ion migration. Large energies associated with the formation of vacancies and interstitials imply that achieving high conductivities will require that defect concentrations are controlled via doping or with compositions that create vacancies or interstitials on the cation sublattice.

Of the compounds investigated, Mg_3NAs, Ca_3NAs, and Ca_3PSb are the most promising. These SEs are predicted to be stable against their respective metal anodes and have percolating barriers for vacancy migration of less than ∼500 meV (∼200 meV for interstitial migration). Stability against oxidation is maintained up to 1.2−1.7 V, implying that interfacial coatings may be needed to achieve compatibility with high-voltage cathodes.

ASSOCIATED CONTENT

Supporting Information

The Supporting Information is available free of charge at https://pubs.acs.org/doi/10.1021/acs.chemmater.1c00096.

Additional details on computational methods; prediction of the ionic radius for Bi^{3-}; composition of Schottky defects; defect formation energies for charged defects; illustration of long-range migration pathway (PDF)

AUTHOR INFORMATION

Corresponding Author

Donald J. Siegel − *Mechanical Engineering Department, Materials Science & Engineering, Applied Physics Program, Joint Center for Energy Storage Research, and University of Michigan Energy Institute, University of Michigan, Ann Arbor, Michigan 48109-2125, United States;* orcid.org/0000-0001-7913-2513; Phone: +1 (734) 764-4808; Email: djsiege@umich.edu

Author

#Kwangnam Kim − *Mechanical Engineering Department, University of Michigan, Ann Arbor, Michigan 48109-2125, United States;* orcid.org/0000-0003-1149-1733

Complete contact information is available at: https://pubs.acs.org/10.1021/acs.chemmater.1c00096

Notes

The authors declare no competing financial interest.

#Present Address: Materials Science Division, Lawrence Livermore National Laboratory, Livermore, California 94550, United States (K.K.).

ACKNOWLEDGMENTS

This work was supported as part of the Joint Center for Energy Storage Research (JCESR), an Energy Innovation Hub funded by the U.S. Department of Energy, Office of Science, Basic Energy Sciences.

REFERENCES

(1) Muldoon, J.; Bucur, C. B.; Gregory, T. Quest for Nonaqueous Multivalent Secondary Batteries: Magnesium and Beyond. *Chem. Rev.* **2014**, *114*, 11683−11720.

(2) Gummow, R. J.; Vamvounis, G.; Kannan, M. B.; He, Y. Calcium-Ion Batteries: Current State-of-the-Art and Future Perspectives. *Adv. Mater.* **2018**, *30*, 1801702.

(3) Kim, D. J.; Yoo, D. J.; Otley, M. T.; Prokofjevs, A.; Pezzato, C.; Owczarek, M.; Lee, S. J.; Choi, J. W.; Stoddart, J. F. Rechargeable Aluminium Organic Batteries. *Nat. Energy* **2019**, *4*, 51−59.

(4) Vardar, G.; Nelson, E. G.; Smith, J. G.; Naruse, J.; Hiramatsu, H.; Bartlett, B. M.; Sleightholme, A. E. S.; Siegel, D. J.; Monroe, C. W. Identifying the Discharge Product and Reaction Pathway for a Secondary Mg/O_2 Battery. *Chem. Mater.* **2015**, *27*, 7564−7568.

(5) Shterenberg, I.; Salama, M.; Yoo, H. D.; Gofer, Y.; Park, J. B.; Sun, Y. K.; Aurbach, D. Evaluation of $(CF_3SO_2)_2N^-$ (TFSI) Based Electrolyte Solutions for Mg Batteries. *J. Electrochem. Soc.* **2015**, *162*, A7118−A7128.

(6) Pan, B.; Zhou, D.; Huang, J.; Zhang, L.; Burrell, A. K.; Vaughey, J. T.; Zhang, Z.; Liao, C. 2,5-Dimethoxy-1,4-Benzoquinone (DMBQ) as Organic Cathode for Rechargeable Magnesium-Ion Batteries. *J. Electrochem. Soc.* **2016**, *163*, A580−A583.

(7) Sun, X.; Bonnick, P.; Duffort, V.; Liu, M.; Rong, Z.; Persson, K. A.; Ceder, G.; Nazar, L. F. A High Capacity Thiospinel Cathode for Mg Batteries. *Energy Environ. Sci.* **2016**, *9*, 2273−2277.
(8) Dong, H.; Liang, Y.; Tutusaus, O.; Mohtadi, R.; Zhang, Y.; Hao, F.; Yao, Y. Directing Mg-Storage Chemistry in Organic Polymers toward High-Energy Mg Batteries. *Joule* **2019**, *3*, 782−793.
(9) Ponrouch, A.; Frontera, C.; Bardé, F.; Palacín, M. R. Towards a Calcium-Based Rechargeable Battery. *Nat. Mater.* **2016**, *15*, 169−172.
(10) Goodenough, J. B.; Kim, Y. Challenges for Rechargeable Li Batteries. *Chem. Mater.* **2010**, *22*, 587−603.
(11) Roth, E. P.; Orendorff, C. J. How Electrolytes Influence Battery Safety. *Electrochem. Soc. Interface* **2012**, *21*, 45−49.
(12) Hu, Y.-S. Batteries: Getting Solid. *Nat. Energy* **2016**, *1*, 16042.
(13) Monroe, C.; Newman, J. The Impact of Elastic Deformation on Deposition Kinetics at Lithium/Polymer Interfaces. *J. Electrochem. Soc.* **2005**, *152*, A396−A404.
(14) Goodenough, J. B.; Singh, P. Review—Solid Electrolytes in Rechargeable Electrochemical Cells. *J. Electrochem. Soc.* **2015**, *162*, A2387−A2392.
(15) Bates, J. B.; Dudney, N. J.; Gruzalski, G. R.; Zuhr, R. A.; Choudhury, A.; Luck, C. F.; Robertson, J. D. Fabrication and Characterization of Amorphous Lithium Electrolyte Thin Films and Rechargeable Thin-Film Batteries. *J. Power Sources* **1993**, *43*, 103.
(16) Hayashi, A.; Hama, S.; Minami, T.; Tatsumisago, M. Formation of Superionic Crystals from Mechanically Milled Li_2S-P_2S_5 Glasses. *Electrochem. Commun.* **2003**, *5*, 111−114.
(17) Murugan, R.; Thangadurai, V.; Weppner, W. Fast Lithium Ion Conduction in Garnet-Type $Li_7La_3Zr_2O_{12}$. *Angew. Chem. Int. Ed.* **2007**, *46*, 7778−7781.
(18) Deiseroth, H.-J.; Kong, S. T.; Eckert, H.; Vannahme, J.; Reiner, C.; Zaiß, T.; Schlosser, M. Li_6PS_5X: A Class of Crystalline Li-Rich Solids with an Unusually High Li^+ Mobility. *Angew. Chem. Int. Ed.* **2008**, *47*, 755−758.
(19) Kamaya, N.; Homma, K.; Yamakawa, Y.; Hirayama, M.; Kanno, R.; Yonemura, M.; Kamiyama, T.; Kato, Y.; Hama, S.; Kawamoto, K.; et al. A Lithium Superionic Conductor. *Nat. Mater.* **2011**, *10*, 682−686.
(20) Kato, Y.; Hori, S.; Saito, T.; Suzuki, K.; Hirayama, M.; Mitsui, A.; Yonemura, M.; Iba, H.; Kanno, R. High-Power All-Solid-State Batteries Using Sulfide Superionic Conductors. *Nat. Energy* **2016**, *1*, 16030.
(21) Manthiram, A.; Yu, X.; Wang, S. Lithium Battery Chemistries Enabled by Solid-State Electrolytes. *Nat. Rev. Mater.* **2017**, *2*, 16103.
(22) Hayashi, A.; Noi, K.; Sakuda, A.; Tatsumisago, M. Superionic Glass-Ceramic Electrolytes for Room-Temperature Rechargeable Sodium Batteries. *Nat. Commun.* **2012**, *3*, 855−856.
(23) Richards, W. D.; Tsujimura, T.; Miara, L. J.; Wang, Y.; Kim, J. C.; Ong, S. P.; Uechi, I.; Suzuki, N.; Ceder, G. Design and Synthesis of the Superionic Conductor $Na_{10}SnP_2S_{12}$. *Nat. Commun.* **2016**, *7*, 11009.
(24) Zhang, Z.; Ramos, E.; Lalère, F.; Assoud, A.; Kaup, K.; Hartman, P.; Nazar, L. F. $Na_{11}Sn_2PS_{12}$: A New Solid State Sodium Superionic Conductor. *Energy Environ. Sci.* **2018**, *11*, 87−93.
(25) Tang, W. S.; Unemoto, A.; Zhou, W.; Stavila, V.; Matsuo, M.; Wu, H.; Orimo, S. I.; Udovic, T. J. Unparalleled Lithium and Sodium Superionic Conduction in Solid Electrolytes with Large Monovalent Cage-like Anions. *Energy Environ. Sci.* **2015**, *8*, 3637−3645.
(26) Yao, Y.-F. Y.; Kummer, J. T. Ion Exchange Properties of and Rates of Ionic Diffusion in Beta-Alumina. *J. Inorg. Nucl. Chem* **1967**, *29*, 2453−2475.
(27) Lu, X.; Bowden, M. E.; Sprenkle, V. L.; Liu, J. A Low Cost, High Energy Density, and Long Cycle Life Potassium-Sulfur Battery for Grid-Scale Energy Storage. *Adv. Mater.* **2015**, *27*, 5915−5922.
(28) Yuan, H.; Li, H.; Zhang, T.; Li, G.; He, T.; Du, F.; Feng, S. A $K_2Fe_4O_7$ Superionic Conductor for All-Solid-State Potassium Metal Batteries. *J. Mater. Chem. A* **2018**, *6*, 8413−8418.
(29) Aubrey, M. L.; Ameloot, R.; Wiers, B. M.; Long, J. R. Metal-Organic Frameworks as Solid Magnesium Electrolytes. *Energy Environ. Sci.* **2014**, *7*, 667−671.
(30) Thelen, J. L.; Inceoglu, S.; Venkatesan, N. R.; Mackay, N. G.; Balsara, N. P. Relationship between Ion Dissociation, Melt Morphology, and Electrochemical Performance of Lithium and Magnesium Single-Ion Conducting Block Copolymers. *Macromolecules* **2016**, *49*, 9139−9147.
(31) Canepa, P.; Bo, S. H.; Sai Gautam, G.; Key, B.; Richards, W. D.; Shi, T.; Tian, Y.; Wang, Y.; Li, J.; Ceder, G. High Magnesium Mobility in Ternary Spinel Chalcogenides. *Nat. Commun.* **2017**, *8*, 1759.
(32) Martinolich, A. J.; Lee, C.-W.; Lu, I.-T.; Bevilacqua, S. C.; Preefer, M. B.; Bernardi, M.; Schleife, A.; See, K. A. Solid-State Divalent Ion Conduction in $ZnPS_3$. *Chem. Mater.* **2019**, *31*, 3652−3661.
(33) Genier, F. S.; Burdin, C. V.; Biria, S.; Hosein, I. D. A Novel Calcium-Ion Solid Polymer Electrolyte Based on Crosslinked Poly(Ethylene Glycol) Diacrylate. *J. Power Sources* **2019**, *414*, 302−307.
(34) Wang, J.; Genier, F. S.; Li, H.; Biria, S.; Hosein, I. D. A Solid Polymer Electrolyte from Cross-Linked Polytetrahydrofuran for Calcium Ion Conduction. *ACS Appl. Polym. Mater.* **2019**, *1*, 1837−1844.
(35) Zhao, Y.; Daemen, L. L. Superionic Conductivity in Lithium-Rich Anti-Perovskites. *J. Am. Chem. Soc.* **2012**, *134*, 15042−15047.
(36) Wang, Y.; Wang, Q.; Liu, Z.; Zhou, Z.; Li, S.; Zhu, J.; Zou, R.; Wang, Y.; Lin, J.; Zhao, Y. Structural Manipulation Approaches towards Enhanced Sodium Ionic Conductivity in Na-Rich Anti-perovskites. *J. Power Sources* **2015**, *293*, 735−740.
(37) Kim, K.; Siegel, D. J. Correlating Lattice Distortions, Ion Migration Barriers, and Stability in Solid Electrolytes. *J. Mater. Chem. A* **2019**, *7*, 3216−3227.
(38) Wang, F.; Evans, H. A.; Kim, K.; Yin, L.; Li, Y.; Tsai, P.-C.; Liu, J.; Lapidus, S. H.; Brown, C. M.; Siegel, D. J.; et al. Dynamics of Hydroxyl Anions Promotes Lithium Ion Conduction in Antiperovskite Li_2OHCl. *Chem. Mater.* **2020**, *32*, 8481−8491.
(39) Li, Y.; Zhou, W.; Xin, S.; Li, S.; Zhu, J.; Lü, X.; Cui, Z.; Jia, Q.; Zhou, J.; Zhao, Y.; et al. Fluorine-Doped Antiperovskite Electrolyte for All-Solid-State Lithium-Ion Batteries. *Angew. Chem. Int. Ed.* **2016**, *55*, 9965−9968.
(40) Lü, X.; Howard, J. W.; Chen, A.; Zhu, J.; Li, S.; Wu, G.; Dowden, P.; Xu, H.; Zhao, Y.; Jia, Q. Antiperovskite Li_3OCl Superionic Conductor Films for Solid-State Li-Ion Batteries. *Adv. Sci.* **2016**, *3*, 1500359.
(41) Lü, X.; Wu, G.; Howard, J. W.; Chen, A.; Zhao, Y.; Daemen, L. L.; Jia, Q. Li-Rich Anti-Perovskite Li_3OCl Films with Enhanced Ionic Conductivity. *Chem. Commun.* **2014**, *50*, 11520−11522.
(42) Kim, K.; Siegel, D. J. Predicting Wettability and the Electrochemical Window of Lithium-Metal/Solid Electrolyte Interfaces. *ACS Appl. Mater. Interfaces* **2019**, *11*, 39940−39950.
(43) He, T.; Huang, Q.; Ramirez, A. P.; Wang, Y.; Regan, K. A.; Rogado, N.; Hayward, M. A.; Haas, M. K.; Slusky, J. S.; Inumara, K.; et al. Superconductivity in the Non-Oxide Perovskite MgCNi3. *Nature* **2001**, *411*, 54−56.
(44) Cao, W. H.; He, B.; Liao, C. Z.; Yang, L. H.; Zeng, L. M.; Dong, C. Preparation and Properties of Antiperovskite-Type Nitrides: $InNNi_3$ and $InNCo_3$. *J. Solid State Chem.* **2009**, *182*, 3353−3357.
(45) Benmalem, Y.; Abbad, A.; Benstaali, W.; Bentounes, H. A.; Seddik, T.; Lantri, T. Thermoelectric, Electronic and Structural Properties of $CuNMn_3$ Cubic Antiperovskite. *J. Comput. Electron.* **2018**, *17*, 881−887.
(46) Chern, M. Y.; Vennos, D. A.; Disalvo, F. J. Synthesis, Structure, and Properties of Anti-Perovskite Nitrides Ca_3MN, M = P, As, Sb, Bi, Ge, Sn, and Pb. *J. Solid State Chem.* **1992**, *96*, 415−425.
(47) Chi, E. O.; Kim, W. S.; Hur, N. H.; Jung, D. New Mg-Based Antiperovskites $PnNMg_3$ (Pn = As, Sb). *Solid State Commun.* **2002**, *121*, 309−312.
(48) Amara, K.; Zemouli, M.; Elkeurti, M.; Belfedal, A.; Saadaoui, F. First-Principles Study of $XNMg_3$ (X = P, As, Sb and Bi) Antiperovskite Compounds. *J. Alloys Compd.* **2013**, *576*, 398−403.

https://dx.doi.org/10.1021/acs.chemmater.1c00096
Chem. Mater. 2021, 33, 2187−2197

(49) Goh, W. F.; Pickett, W. E. Survey of the Class of Isovalent Antiperovskite Alkaline-Earth Pnictide Compounds. *Phys. Rev. B* **2018**, *97*, 35202.
(50) Bilal, M.; Jalali-Asadabadi, S.; Ahmad, R.; Ahmad, I. Electronic Properties of Antiperovskite Materials from State-of-the-Art Density Functional Theory. *J. Chem.* **2015**, *2015*, 1.
(51) Kirchner, M.; Schnelle, W.; Wagner, F. R.; Niewa, R. Preparation, Crystal Structure and Physical Properties of Ternary Compounds (R_3N)In, R = Rare-Earth Metal. *Solid State Sci.* **2003**, *5*, 1247−1257.
(52) Velden, A.; Jansen, M. Zur Kenntnis Der Inversen Perowskite M_3TO (M = Ca, Sr, Yb; T = Si, Ge, Sn, Pb). *Zeitschrift fur Anorg. und Allg. Chemie* **2004**, *630*, 234−238.
(53) Okamoto, Y.; Sakamaki, A.; Takenaka, K. Thermoelectric Properties of Antiperovskite Calcium Oxides Ca_3PbO and Ca_3SnO. *J. Appl. Phys.* **2016**, *119*, 205106.
(54) Chen, K.; Li, C.; Hu, M.; Hou, X.; Li, C.; Chen, Z. Deformation Modes and Anisotropy of Anti-Perovskite Ti_3AN (A = Al, In and Tl) from First-Principle Calculations. *Materials* **2017**, *10*, 362.
(55) Quintela, C. X.; Campbell, N.; Shao, D. F.; Irwin, J.; Harris, D. T.; Xie, L.; Anderson, T. J.; Reiser, N.; Pan, X. Q.; Tsymbal, E. Y.; et al. Epitaxial Thin Films of Dirac Semimetal Antiperovskite Cu_3PdN. *APL Mater.* **2017**, *5*, No. 096103.
(56) Suetsugu, S.; Hayama, K.; Rost, A. W.; Nuss, J.; Mühle, C.; Kim, J.; Kitagawa, K.; Takagi, H. Magnetotransport in Sr_3PbO Antiperovskite. *Phys. Rev. B* **2018**, *98*, 115203.
(57) Hausmann, J. N.; Oudah, M.; Ikeda, A.; Yonezawa, S.; Maeno, Y. Controlled Synthesis of the Antiperovskite Oxide Superconductor $Sr_{3-x}SnO$. *Supercond. Sci. Technol.* **2018**, *31*, No. 055012.
(58) Chern, M. Y.; Disalvo, F. J.; Parise, J. B.; Goldstone, J. A. The Structural Distortion of the Anti-Perovskite Nitride Ca_3AsN. *J. Solid State Chem.* **1992**, *96*, 426−435.
(59) Kresse, G.; Furthmüller, J. Efficient Iterative Schemes for Ab Initio Total-Energy Calculations Using a Plane-Wave Basis Set. *Phys. Rev. B* **1996**, *54*, 11169.
(60) Perdew, J. P.; Burke, K.; Ernzerhof, M. Generalized Gradient Approximation Made Simple. *Phys. Rev. Lett.* **1996**, *77*, 3865−3868.
(61) Blöchl, P. E. Projector Augmented-Wave Method. *Phys. Rev. B* **1994**, *50*, 17953−17979.
(62) Kresse, G.; Joubert, D. From Ultrasoft Pseudopotentials to the Projector Augmented-Wave Method. *Phys. Rev. B* **1999**, *59*, 1758−1775.
(63) Murnaghan, F. D. The Compressibility of Media under Extreme Pressures. *Proc. Natl. Acad. Sci. U. S. A* **1944**, *30*, 244−247.
(64) Heyd, J.; Scuseria, G. E.; Ernzerhof, M. Hybrid Functionals Based on a Screened Coulomb Potential. *J. Chem. Phys.* **2003**, *118*, 8207−8215.
(65) Krukau, A. V.; Vydrov, O. A.; Izmaylov, A. F.; Scuseria, G. E. Influence of the Exchange Screening Parameter on the Performance of Screened Hybrid Functionals. *J. Chem. Phys.* **2006**, *125*, 224106.
(66) Shishkin, M.; Kresse, G. Implementation and Performance of the Frequency-Dependent GW Method within the PAW Framework. *Phys. Rev. B* **2006**, *74*, No. 035101.
(67) Shishkin, M.; Kresse, G. Self-Consistent GW Calculations for Semiconductors and Insulators. *Phys. Rev. B* **2007**, *75*, 235102.
(68) Fuchs, F.; Furthmüller, J.; Bechstedt, F.; Shishkin, M.; Kresse, G. Quasiparticle Band Structure Based on a Generalized Kohn-Sham Scheme. *Phys. Rev. B* **2007**, *76*, 115109.
(69) Jónsson, H.; Mills, G.; Jacobsen, K. W. Nudged Elastic Band Method for Finding Minimum Energy Paths of Transitions. In *Classical and Quantum Dynamics in Condensed Phase Simulations*; Berne, B. J., Ciccotti, G., Coker, D. F., Eds.; World Scientific: Singapore, 1998; pp. 385−404.
(70) Henkelman, G.; Jónsson, H. Improved Tangent Estimate in the Nudged Elastic Band Method for Finding Minimum Energy Paths and Saddle Points. *J. Chem. Phys.* **2000**, *113*, 9978−9985.
(71) Voigt, W. *Lehrbuch Der Kristallphysik*; Taubner: Leipzig, 1928.
(72) Van de Walle, C. G.; Neugebauer, J. First-Principles Calculations for Defects and Impurities: Applications to III-Nitrides. *J. Appl. Phys.* **2004**, *95*, 3851−3879.
(73) Makov, G.; Payne, M. C. Periodic Boundary Conditions in Ab Initio Calculations. *Phys. Rev. B* **1995**, *51*, 4014−4022.
(74) Komsa, H.-P.; Rantala, T. T.; Pasquarello, A. Finite-Size Supercell Correction Schemes for Charged Defect Calculations. *Phys. Rev. B* **2012**, *86*, No. 045112.
(75) Ong, S. P.; Wang, L.; Kang, B.; Ceder, G. Li−Fe−P−O_2 Phase Diagram from First Principles Calculations. *Chem. Mater.* **2008**, *20*, 1798−1807.
(76) Ong, S. P.; Jain, A.; Hautier, G.; Kang, B.; Ceder, G. Thermal Stabilities of Delithiated Olivine MPO_4 (M=Fe, Mn) Cathodes Investigated Using First Principles Calculations. *Electrochem. Commun.* **2010**, *12*, 427−430.
(77) Jain, A.; Ong, S. P.; Hautier, G.; Chen, W.; Richards, W. D.; Dacek, S.; Cholia, S.; Gunter, D.; Skinner, D.; Ceder, G.; et al. Commentary: The Materials Project: A Materials Genome Approach to Accelerating Materials Innovation. *APL Mater.* **2013**, *1*, No. 011002.
(78) Ong, S. P.; Richards, W. D.; Jain, A.; Hautier, G.; Kocher, M.; Cholia, S.; Gunter, D.; Chevrier, V. L.; Persson, K. A.; Ceder, G. Python Materials Genomics (Pymatgen): A Robust, Open-Source Python Library for Materials Analysis. *Comput. Mater. Sci.* **2013**, *68*, 314−319.
(79) Zhu, Y.; He, X.; Mo, Y. Origin of Outstanding Stability in the Lithium Solid Electrolyte Materials: Insights from Thermodynamic Analyses Based on First-Principles Calculations. *ACS Appl. Mater. Interfaces* **2015**, *7*, 23685−23693.
(80) Emsley, J. *The Elements*, 3rd ed.; Oxford University Press: New York, 1998.
(81) Sreedevi, P. D.; Ravindran, P.; Vidya, R. First Principles Prediction of the Ground State Crystal Structures of Antiperovskite Compounds A_3PN (A= Be, Mg, Ca, Sr, Ba and Zn). *Mater. Today Proc.* **2019**, *8*, 294−300.
(82) Zhang, Y.; Zhao, Y.; Chen, C. Ab Initio Study of the Stabilities of and Mechanism of Superionic Transport in Lithium-Rich Antiperovskites. *Phys. Rev. B* **2013**, *87*, 134303.
(83) Emly, A.; Kioupakis, E.; Van der Ven, A. Phase Stability and Transport Mechanisms in Antiperovskite Li_3OCl and Li_3OBr Superionic Conductors. *Chem. Mater.* **2013**, *25*, 4663−4670.
(84) Mouta, R.; Melo, M. Á. B.; Diniz, E. M.; Paschoal, C. W. A. Concentration of Charge Carriers, Migration, and Stability in Li_3OCl Solid Electrolytes. *Chem. Mater.* **2014**, *26*, 7137−7144.
(85) Mouta, R.; Diniz, E. M.; Paschoal, C. W. A. Li^+ Interstitials as the Charge Carriers in Superionic Lithium-Rich Anti-Perovskites. *J. Mater. Chem. A* **2015**, *4*, 1586−31590.
(86) Lu, Z.; Chen, C.; Baiyee, Z. M.; Chen, X.; Niu, C.; Ciucci, F. Defect Chemistry and Lithium Transport in Li_3OCl Anti-Perovskite Superionic Conductors. *Phys. Chem. Chem. Phys.* **2015**, *17*, 32547−32555.
(87) Stegmaier, S.; Voss, J.; Reuter, K.; Luntz, A. C. Li^+ Defects in a Solid-State Li Ion Battery: Theoretical Insights with a Li_3OCl Electrolyte. *Chem. Mater.* **2017**, *29*, 4330−4340.
(88) Rong, Z.; Malik, R.; Canepa, P.; Sai Gautam, G.; Liu, M.; Jain, A.; Persson, K.; Ceder, G. Materials Design Rules for Multivalent Ion Mobility in Intercalation Structures. *Chem. Mater.* **2015**, *27*, 6016−6021.
(89) Jansen, M. Volume Effect or Paddle-Wheel Mechanism - Fast Alkali-Metal Ionic Conduction in Solids with Rotationally Disordered Complex Anions. *Angew. Chem. Int. Ed. Engl.* **1991**, *30*, 1547−1558.
(90) Tilley, R. J. D. *Defects in Solids*; John Wiley & Sons, Inc.: Hoboken, NJ, USA, 2008.
(91) Charles, K. *Introduction to Solid State Physics*, 8 th ed.; John Wiley & Sons: New York, 2005.
(92) Smith, J. G.; Naruse, J.; Hiramatsu, H.; Siegel, D. J. Intrinsic Conductivity in Magnesium−Oxygen Battery Discharge Products: MgO and MgO_2. *Chem. Mater.* **2017**, *29*, 3152−3163.

https://dx.doi.org/10.1021/acs.chemmater.1c00096
Chem. Mater. 2021, 33, 2187−2197

(93) Kim, C.; Phillips, P. J.; Key, B.; Yi, T.; Nordlund, D.; Yu, Y.-S.; Bayliss, R. D.; Han, S.-D.; He, M.; Zhang, Z.; et al. Direct Observation of Reversible Magnesium Ion Intercalation into a Spinel Oxide Host. *Adv. Mater.* **2015**, *27*, 3377−3384.
(94) Sa, N.; Kinnibrugh, T. L.; Wang, H.; Sai Gautam, G.; Chapman, K. W.; Vaughey, J. T.; Key, B.; Fister, T. T.; Freeland, J. W.; Proffit, D. L.; et al. Structural Evolution of Reversible Mg Insertion into a Bilayer Structure of V_2O_5· n H_2O Xerogel Material. *Chem. Mater.* **2016**, *28*, 2962−2969.
(95) Lipson, A. L.; Pan, B.; Lapidus, S. H.; Liao, C.; Vaughey, J. T.; Ingram, B. J. Rechargeable Ca-Ion Batteries: A New Energy Storage System. *Chem. Mater.* **2015**, *27*, 8442−8447.
(96) Tchitchekova, D. S.; Frontera, C.; Ponrouch, A.; Krich, C.; Bardé, F.; Palacín, M. R. Electrochemical Calcium Extraction from 1D-$Ca_3Co_2O_6$. *Dalton Trans.* **2018**, *47*, 11298−11302.
(97) Verrelli, R.; Black, A. P.; Pattanathummasid, C.; Tchitchekova, D. S.; Ponrouch, A.; Oró-Solé, J.; Frontera, C.; Bardé, F.; Rozier, P.; Palacín, M. R. On the Strange Case of Divalent Ions Intercalation in V_2O_5. *J. Power Sources* **2018**, *407*, 162−172.
(98) Yu, S.; Park, H.; Siegel, D. J. Thermodynamic Assessment of Coating Materials for Solid-State Li, Na, and K Batteries. *ACS Appl. Mater. Interfaces* **2019**, *11*, 36607−36615.
(99) Chen, T.; Ceder, G.; Sai Gautam, G.; Canepa, P. Evaluation of Mg Compounds as Coating Materials in Mg Batteries. *Front. Chem.* **2019**, *7*, 24.
(100) Kumar, N.; Siegel, D. J. Interface-Induced Renormalization of Electrolyte Energy Levels in Magnesium Batteries. *J. Phys. Chem. Lett.* **2016**, *7*, 874−881.
(101) Park, H.; Yu, S.; Siegel, D. J. Predicting Charge Transfer Stability between Sulfide Solid Electrolytes and Li Metal Anodes. *ACS Energy Lett.* **2021**, *6*, 150−157.
(102) Thompson, T.; Yu, S.; Williams, L.; Schmidt, R. D.; Garcia-Mendez, R.; Wolfenstine, J.; Allen, J. L.; Kioupakis, E.; Siegel, D. J.; Sakamoto, J. Electrochemical Window of the Li-Ion Solid Electrolyte $Li_7La_3Zr_2O_{12}$. *ACS Energy Lett.* **2017**, *2*, 462−468.
(103) Yu, S.; Schmidt, R. D.; Garcia-Mendez, R.; Herbert, E.; Dudney, N. J.; Wolfenstine, J. B.; Sakamoto, J.; Siegel, D. J. Elastic Properties of the Solid Electrolyte $Li_7La_3Zr_2O_{12}$ (LLZO). *Chem. Mater.* **2016**, *28*, 197−206.
(104) Wolfenstine, J.; Allen, J. L.; Sakamoto, J.; Siegel, D. J.; Choe, H. Mechanical Behavior of Li-Ion-Conducting Crystalline Oxide-Based Solid Electrolytes: A Brief Review. *Ionics* **2018**, *24*, 1271−1276.
(105) Sakuda, A.; Hayashi, A.; Takigawa, Y.; Higashi, K.; Tatsumisago, M. Evaluation of Elastic Modulus of Li_2S-P_2S_5 Glassy Solid Electrolyte by Ultrasonic Sound Velocity Measurement and Compression Test. *J. Ceram. Soc. Jpn.* **2013**, *121*, 946−949.
(106) Garcia-Mendez, R.; Smith, J. G.; Neuefeind, J. C.; Siegel, D. J.; Sakamoto, J. Correlating Macro and Atomic Structure with Elastic Properties and Ionic Transport of Glassy Li_2S-P_2S_5 (LPS) Solid Electrolyte for Solid-State Li Metal Batteries. *Adv. Energy Mater.* **2020**, *10*, 2000335.
(107) Samsonov, G. V. *Handbook of the Physicochemical Properties of the Elements*; IFI-Plenum: New York, 1968.
(108) Kaye, G. W. C.; Laby, T. H. *Tables of Physical and Chemical Constants*, 15 th ed.; Longman: London, 1993.
(109) Nagy, K. S.; Siegel, D. J. Anisotropic Elastic Properties of Battery Anodes. *J. Electrochem. Soc.* **2020**, *167*, 110550.
(110) Yu, S.; Siegel, D. J. Grain Boundary Softening: A Potential Mechanism for Lithium Metal Penetration through Stiff Solid Electrolytes. *ACS Appl. Mater. Interfaces* **2018**, *10*, 38151−38158.

https://dx.doi.org/10.1021/acs.chemmater.1c00096
Chem. Mater. 2021, 33, 2187−2197